Revisiting Ray-Tracing Algorithm for Future Limb-Scanning Missions

Francesco Pio De Cosmo[1,2(✉)] and Luca Sgheri[2]

[1] Department of Information Engineering, University of Florence, Florence, Italy
[2] National Research Council, Institute for Applied Calculus, Sesto Fiorentino, Italy
francescopio.decosmo@unifi.it, luca.sgheri@fi.iac.cnr.it

Abstract. In the forward model for limb-scanning instruments, ray tracing must be accounted for because variations in air refractivity cause the lines of sight to bend from straight paths into curves. The tangent point of a line of sight defined as the minimum height, depends on both the instrument's nadir angle and the atmospheric state. To achieve reliable tangent point determination, the off-nadir angles must be calibrated to account for Earth's ellipsoidal geometry and realistic atmospheric conditions sampled by these lines of sight paths. In this study, we improve the ray-tracing algorithm originally developed for MIPAS operational retrievals. The algorithm is applied to more accurately assess the impact of atmospheric variability on the relationship between off-nadir angles and tangent point localization. It also allows us to estimate the smoothing error associated with the coarse horizontal sampling of the MIPAS observation pattern. We used a configuration representative of the proposed CAIRT mission instrument as a case scenario for future instruments such as the STRIVE mission by NASA.

Keywords: Remote sensing · CAIRT · Ray tracing algorithm · Limb scanning

1 Introduction

Limb scanning is an observation geometry in which the instrument looks tangentially through the atmosphere, without intersecting the Earth's surface. Compared to nadir-viewing satellites that observe vertically toward the Earth's surface, limb sounders achieve much higher vertical resolution, offering more detailed information on the upper atmosphere. In contrast, nadir looking instrument, have limited sensitivity to changes in the upper layers composition, as the signal from higher altitudes is largely masked by the stronger contributions coming from the lower layers.

However, limb instruments face two problems. First, the mechanics of the instrument is normally more complicated with respect to a nadir looking instrument, because it needs more complex optics [4]. Second, from the point of view of the forward modeling and retrieval procedures, there is the additional complications due to predict the shape of the lines of sight, since the changes in the

© The Author(s), under exclusive license to Springer Nature Switzerland AG 2027
O. Gervasi et al. (Eds.): ICCSA 2026 Workshops, LNCS 16766, pp. 153–170, 2027.
https://doi.org/10.1007/978-3-032-30539-8_10

atmosphere refractive index bend the rays from straight lines into curves. This makes it necessary to accurately determine the tangent points, where the line of sight is closest to the Earth, in order to correctly assign altitudes to the retrieved atmospheric profiles.

Only a limited number of limb-scanning instruments have operated in space. On ESA's ENVISAT mission (2002–2012), SCIAMACHY (*Scanning Imaging Absorption Spectrometer for Atmospheric Cartography*) [5] and MIPAS (*Michelson Interferometer for Passive Atmospheric Sounding*) [12] provided valuable measurements, with MIPAS delivering geolocated profiles of temperature, pressure, and up to 20 atmospheric gases from 6 to 60 km altitude [8,21]. Other notable instruments include ACE-FTS (*Atmospheric Chemistry Experiment – Fourier Transform Spectrometer*) on Canada's SCISAT (2003) [2] and MLS (*Microwave Limb Sounder*) on NASA's Aura (2004) [28], which have supplied high-quality vertical profiles of atmospheric composition, temperature, and dynamics in the last two decades. However, both ACE-FTS and MLS are now nearing the end of their operational lifetimes.

The projected CAIRT (*Changing-Atmosphere Infra-Red Tomography Explorer*) instrument [26] instrument was conceived as a limb-scanning instrument and a potential successor to MIPAS. Although it was not selected for the 11th Earth Explorer mission in the final User Consultation Meeting, CAIRT provides a valuable framework for testing methodological advances, both in hardware and in software, for future limb-scanning missions. CAIRT was designed to acquire continuous measurements along the satellite orbit, with each acquisition capturing a 2D set of limb-emission spectra via individual detector pixels. The vertical coverage extends from about 5 km up to 115 km, with a vertical resolution of about 1 km up to the mid-mesosphere and 2 km above. The horizontal coverage extends over a swath of about 500 km, with along-track sampling of about 50 km and across-track sampling of 50 km. Further details on the instrument characteristics are described in the Mission Report [10].

Recently, the STRIVE (Stratosphere Troposphere Response using Infrared Vertically-resolved light Explorer) mission [27] has been selected for continued development by NASA. The mission contains ALICE (Advanced Limb Infrared Chemistry Experiment), an infrared limb-scanner that has many similarities with the CAIRT project.

In the forward model for limb-scanning instruments, the ray tracing must be taken into account. The retrieved lines of sight, and thus the accuracy of the tangent point positions, depend on several factors: the numerical ray-tracing method, the atmospheric refractive index model, and the assumed atmospheric composition. As suggested by the work [24] for MIPAS, variations in the ray-tracing method or refractive index model produce negligible errors ($\lesssim$ 2 m), suggesting that the choice of atmospheric model may have a more significant effect on the accuracy of tangent point determination and, consequently, of the retrieved profiles.

In this paper, we extend this study by implementing an improved ray-tracing algorithm originally developed for MIPAS operational retrievals. Using this algo-

rithm we provide a more accurate analysis of the relationship between instrument off-nadir angles and tangent point altitudes. In particular, we focus on the effect of using real atmospheric refractivity data, including seasonal variations, rather than standard models, which may introduce significant uncertainties in tangent point determination. This approach also allows us to estimate the smoothing error associated with the coarse horizontal sampling of the MIPAS observation pattern, which can now be assessed using a finer atmospheric discretization.

In Sect. 2, we provide a brief overview of ray tracing and the key aspects involved. Section 3 presents a methodology for predicting the instrument off-nadir angles without a priori knowledge of the sampled atmosphere. In Sect. 4, we report the main results of our analysis about displacements in tangent point localization Subsect. 4.1. In Subsect. 4.2, we estimate the MIPAS smoothing error due to the instrument's coarse horizontal resolution as an additional application of the algorithm. Finally, in Sect. 5 we derive some conclusions and ideas for the path ahead. In Appendix A we provide a brief description of the satellite orbit and atmospheric grid, as well as the geometry of the lines of sight adopted in the simulations.

2 Ray Tracing

2.1 Atmospheric Refractivity Models

The line of sight (LoS) is the trajectory of an electromagnetic ray, governed by the atmospheric refractive index n. Since n exceeds unity only slightly, it is convenient to define the refractivity $N = n - 1$ to quantify this deviation. Ray propagation in such a medium is described by the Eikonal equation [3], which is derived from the wave equation under the approximation that n varies slowly with respect to the radiation wavelength [1], as is the case of the infrared band. The LoSs are then the solution of this equation, that can be written as:

$$\frac{d}{ds}\left(n\big(\mathbf{L}(s)\big)\frac{d\mathbf{L}(s)}{ds}\right) = \nabla n\big(\mathbf{L}(s)\big), \tag{1}$$

where s is the arc parameter and $\mathbf{L}(s)$ represents the LoS. The refractive index n is mainly governed by air density and can be computed using standard models of atmospheric refraction. The Edlén model [9] calculates the refractivity as

$$n - 1 = \left(\frac{\rho_a}{\rho_{a,\mathrm{st}}}\right) N_{a,\mathrm{st}}(\lambda), \tag{2}$$

where the refractivity depends linearly on the atmospheric dry air density ρ_a, scaled by a standard density $\rho_{a,\mathrm{st}}$ at sea-level conditions ($p_{\mathrm{st}} = 1013.25$ hPa, $T_{\mathrm{st}} = 273.15$ K). Here, $N_{a,\mathrm{st}}$ represents the specific refractivity of dry air at standard conditions and depends on the wavelength λ . However, this simple model does not account for the effect of water vapor.

Ciddor [6] provides a more accurate formulation that includes the dependence on water vapor content and CO_2 concentration. According to Mathar [17], the

Ciddor method achieves an accuracy of about 10^{-6} in the refractive index for wavelengths up to 25 mm, covering the full relevant infrared spectral range. The refractivity, calculated following the Ciddor formulation, is expressed as

$$n - 1 = \left(\frac{\rho_a}{\rho_{a,\mathrm{st}}}\right) N_{a,\mathrm{st}}(\lambda) + \left(\frac{\rho_w}{\rho_{w,\mathrm{st}}}\right) N_{w,\mathrm{st}}(\lambda), \tag{3}$$

where ρ_a and ρ_w are the actual densities of dry air and water vapor under the given atmospheric conditions, $\rho_{a,\mathrm{st}}$ and $\rho_{w,\mathrm{st}}$ correspond to these at standard temperature and pressure values and $N_{a,\mathrm{st}}$, $N_{w,\mathrm{st}}$ are the specific refractivities of dry air and water vapor at standard reference conditions and wavelength. In this formulation, $N_{a,\mathrm{st}}$ also introduces a dependence on the CO_2 concentration. For both methods we chose a representative mid-infrared wavelength 10 mm, and a CO_2 mixing ratio of 425 ppmv for the Ciddor method, that is the one that we adopt in this study.

2.2 Geometric Configuration and Numerical Approach

A common and reasonable assumption is that the satellite's orbit around Earth can be approximated as circular. This approximation is justified by the requirement for the satellite to maintain an almost constant altitude above the Earth's surface [11], so the orbit eccentricity must be low. Also, the orbit is chosen to be sun-synchronous, that ensures that the satellite passes over any given point on Earth at nearly the same local solar time. For the Earth's shape, we chose to adopt the WGS84 rotational ellipsoid [19]. A more detailed discussion of the geometric considerations is given in Appendix A. For the ray-tracing procedure, a model of the atmosphere must be selected, including at least pressure, temperature and water vapor as a function of the orbital coordinate and the altitude above the WGS84 surface. In the present study, two distinct models were considered:

- The *US Standard Atmosphere 1976* (US76) [20], representing a reference standard atmosphere that provides globally averaged conditions. This model atmosphere does not depend on the geolocation or time.
- The atmosphere from the *ERA5 reanalysis dataset* [13], representing a realistic atmosphere including profiles of pressure, temperature, water vapour, and CO_2 from CAMS [7], extended up to 120 km using the IG2 climatology [23]. This model is used to represent the *true* atmospheric state.

For the numerical implementation of the Eikonal Eq. (1), we adopt the Adaptive Eikonal (AEIK) method described in [24], which employs a multi-step predictor-corrector approach and an adaptive step size based on the curvature of the line of sight. This allows for larger step sizes (up to 1 km) in regions with low atmospheric density, while reducing the step size to as small as 10 m in denser layers. The LoS tracing is performed using a backward ray-tracing algorithm. Starting from the satellite position, propagated through the atmosphere according to the solution of the Eikonal equation, reaching the tangent point at

its minimum altitude, and subsequently followed until it exits the atmospheric domain. We revisited the MIPAS ray-tracing algorithm and we improved the numerical stability of the solution method.

3 Methods

3.1 Determination of the Off-Nadir Angles

The off-nadir angles, or pointing angles, are defined as the angles between the direction of the satellite detectors and the line from the satellite normal to the Earth's surface. These angles are determined a-priori to ensure that the lines of sight intersect a predefined set of target *engineering* tangent altitudes, which defines the instrument's viewing geometry. The relationship between off-nadir angles and tangent height, however, are influenced by the Earth eccentricity and the atmospheric composition sampled by the line of sight. The Earth curvature, at least the value predicted by the WGS84 model, is known and can therefore be accounted for in advance. On the other hand the actual atmospheric composition is only known after the retrieval operation. But the off-nadir angles must be predeterminated, requiring an approximation of the atmosphere, which naturally introduces a bias between the actual tangent altitudes reached and the target *engineering* tangent altitudes. This choice influences the magnitude of the bias, as it will be shown in Sect. 4.

To account for the Earth's ellipticity, the adjustment of the off-nadir angles depends on the instrument hardware. The MIPAS instrument used a sequential acquisition of the sweeps, so each off-nadir angle could be separately adjusted [8]. The CAIRT instrument foresaw a global pitch adjustment [10] to counter variations of tangent altitudes along the orbit. Other instrumental models might provide different adjustment techniques. In this study we assume to be able to determine each off-nadir angle separately. Based on this assumption, we now describe the method we adopted to account for the Earth shape, which can be treated a priori, before performing ray tracing. We only consider a single set of off-nadir angles, restricting the ray-tracing to the orbital plane, as already mentioned. This approach is consistent with the planned retrieval procedure for CAIRT, which operates independently for each along-track line of sight (Fig. 1).

The goal is to determine the off-nadir angles $\{\hat{\alpha}_i\}_{i=1,\ldots,N}$, where N corresponds to the number of detectors, that produce tangent altitudes as close as possible to $\{\hat{h}_i\}_{i=1,\ldots,N}$, taking into account variations in the Earth's ellipticity as a function of the satellite position during each acquisitions.

The strategy employed to determine $\{\hat{\alpha}_i\}$ from the sampled $\{\hat{h}_i\}$ is the following:

(i) We define a preliminary set of m candidate off-nadir angles $\{\alpha_i\}_{i=1,\ldots,m}$ sampled from the interval $[\alpha_{\min}, \alpha_{\max}]$, with $\alpha_{\min} = 61°$ and $\alpha_{\max} = 65°$, chosen conservatively to ensure that rays remain within the atmosphere and do not intersect the Earth's surface [10].

$$\alpha_1 = \alpha_{\min}, \ \ldots, \ \alpha_M = \alpha_{\max}. \tag{4}$$

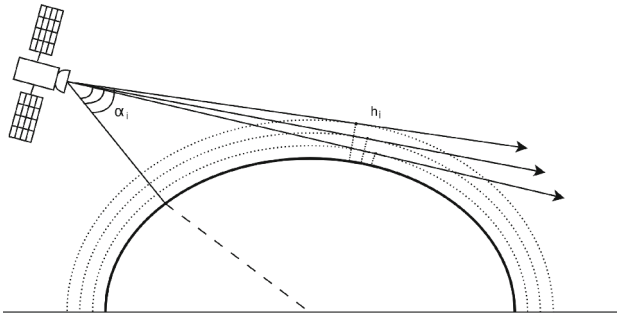

Fig. 1. Schematic of the satellite viewing geometry, showing off-nadir angles $\{\alpha_i\}$ and their corresponding tangent points $\{h_i\}$ for a fixed satellite acquisition.

This sampling does not need to be uniform and is independent of the particular satellite acquisition.

(ii) We define a set of satellite positions along the orbit, corresponding to sequential satellite acquisition and indexed by $j = 1, \ldots, N_{\text{acq}}$.

(iii) For each acquisition j, we trace the lines of sight $\mathbf{L}(s)_{ij}$ corresponding to the set $\{\alpha_i\}$, obtaining a new set of tangent altitudes candidate $\{h_{ij}\}$. We then define a linear spline $s_j(h)$ built using the nodes:

$$(h_{ij}, \alpha_i), \quad i = 1, \ldots, m \qquad j = 1, \ldots, N_{\text{acq}}. \tag{5}$$

(iv) Finally, for each acquisition j, evaluate the spline at the selected engineering tangent altitudes $\{\hat{h}_i\}$ to obtain the required off-nadir angles:

$$\hat{\alpha}_{ij} = s_j(\hat{h}_i), \quad i = 1, \ldots, N \qquad 1, \ldots, m \qquad j = 1, \ldots, N_{\text{acq}}. \tag{6}$$

3.2 Characterization of a Atmospheric Model

An atmospheric model is then required to apply the procedure described in the previous section. Two possible choices have been made.

- **Geometric model:** The lines of sight are computed using a straight-line approach, neglecting the bending effect of atmospheric refraction.
- **Standard US76 model:** The lines of sight are computed assuming a standard US76 atmosphere, a globally uniform atmospheric model.

The a priori tangent points and off-nadir angles reported by the instruments are determined differently: ACE-FTS [18] and MLS [22] provide geometric (*unrefracted*) values derived from the instrument pointing, without explicitly accounting for atmospheric refraction, whereas MIPAS [15] estimates these angles using the standard US76 atmospheric model, which includes refractive effects.

This choice directly affects the curvature of the line of sight, and consequently the altitude and location of the tangent point, whose prediction accuracy depends primarily on the assumed atmospheric model, as already shown in [24].

Once the atmospheric model is fixed, the corresponding off-nadir angles can be predetermined and used as input to value the accuracy of the tangent point prediction. To include the effects of the atmosphere in the ray-tracing computation, the atmospheric properties must first be discretized on a suitable grid, as detailed in Appendix A. The accuracy is then estimated as the displacement between the predicted tangent point and the actual tangent point computed using the ERA5 reanalysis data, taken as the reference *true* atmosphere. This displacement can be decomposed into a vertical shift in altitude, and an horizontal displacement along the angular level line. We focus on the tangent altitudes lower than 20 km, where the influence of the atmosphere is more significant and the curvature of the ray path is more pronounced [16]. Above this altitude, the effect of atmospheric refraction becomes negligible, as the lines of sight traverse less dense layers with smaller variations in the refractive index.

4 Results

In this section, we present two results obtained with the new ray-tracing algorithm. First, we evaluate the accuracy of tangent-points prediction depending on the Earth atmospheric model used to determine the off-nadir angles, following the methodology illustrated in Sect. 3 and using the CAIRT acquisition pattern as an example framework. Second, we demonstrate an independent application: the algorithm is used to estimate the MIPAS smoothing error resulting from the instrument's low horizontal resolution

4.1 Accuracy of the Tangent Point Prediction

In order to quantify the accuracy of the tangent points, we selected a test sun-synchronous orbit inclined at 98.7° to the equatorial plane, with an average altitude of 830 km, the ascending node at a latitude of 0°, and the UTC time of July 10, 2021, 12:00:00. We then applied the procedure of Sect. 3.1 to determine the off-nadir angles corresponding to the engineering tangent altitudes $\{5, 10, 15, 20\}$ km, using both the geometric and US76 atmosphere for the calculation. Then we performed the ray tracing using the *true* ERA5 atmosphere and measured the displacement of the tangent point. In the left panel of Fig. 2, we show the tangent altitudes obtained for the geometric model (dashed lines) and the US76 model (solid lines). These values are plotted as a function of the satellite polar coordinate in the orbital plane, which indicates the satellite's position along its circular orbit. A tolerance band of 500 m is also shown; this value corresponds to the goal of the *absolute geometric knowledge* as specified in the CAIRT Mission Required Document [10]. In the right panel, we show a zoom of the tangent altitudes predicted using the US76 model, in order to appreciate the variations.

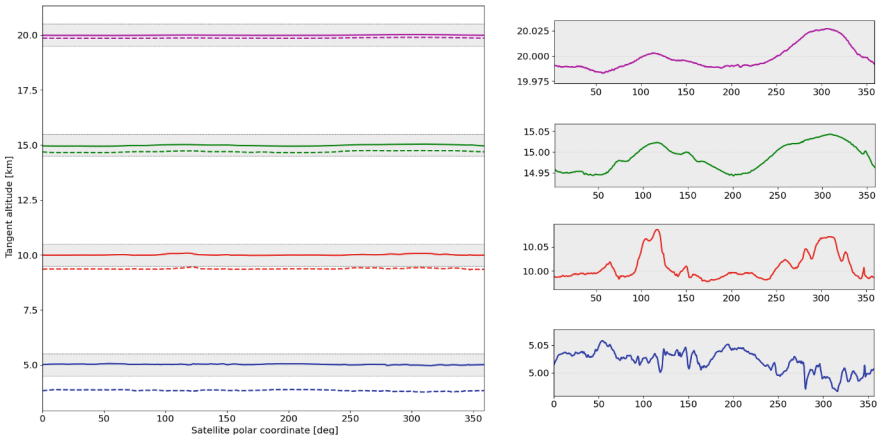

Fig. 2. Variation of the tangent altitude as a function of the satellite polar coordinate for a test orbit. Left panel: tangent altitudes obtained with the reference atmosphere along the orbit when the off-nadir angles are estimated with the geometric model (dashed line) and with the US76 model (solid line). A tolerance of 500 m is also shown. Right panel: zoom of the US76 plots

As shown in the figure, and as expected, the predictions from the geometric model are less accurate than those made with the US76 model. The off-nadir angles required to reach the engineering tangent altitudes are underestimated in the geometric model, as the curvature effect of the atmosphere is not accounted for. Consequently, the tangent point altitudes exhibit a negative bias. In detail, a line of sight starting from off-nadir angles that do not account for atmospheric refraction, reach tangent heights that, under realistic atmospheric conditions, are displaced by approximately 50 m at 20 km, increasing up to 1 km at 5 km relative to the predicted values.

These results indicate that the approximation introduced by the geometric model is too coarse, so we examine the US76 model. In Fig. 3 we show the vertical displacement using an extended range of engineering talgent altitudes from 5 to 40 km, with a 1 km step. As expected, the differences statistically increase when the engineering tangent altitude decrease, because the line of sight samples the lower and denser atmospheric layers. There are some exceptions due to the local atmospheric composition, for instance the maximal displacement of approximately 100 m is reached for the 10 km engineering tangent altitude.

The displacement of the tangent points can be measured not only through the vertical difference, as shown so far, but also through the polar coordinate difference, which provides complementary spatial information. Since the ray tracing is confined to the orbital plane, we can use the two dimensional coordinate system using φ, its angle along the Earth's elliptical surface, and z, its altitude above the Earth WGS84 surface, see Appendix A for more details. The polar displacement is then computed at a fixed engineering altitude as the length of

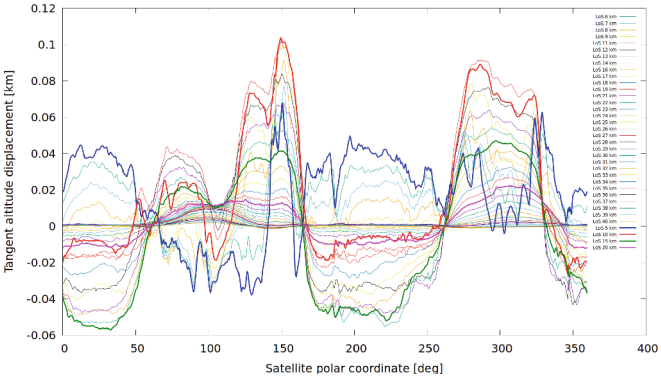

Fig. 3. Tangent altitude vertical displacement as a function of the polar coordinate of the satellite. The tangent altitudes considered in the previous figure are highlighted with a thicker line, and the color is maintained.

the arc between the angle φ of the engineering tangent point and that of the tangent point obtained with the ERA5 atmosphere.

We selected a sample of 14 consecutive orbits at the same UTC times as in the previous case, covering different latitude bands to provide a representative sampling of the whole Earth. Just as in the previous case, we focused on the $\{5, 10, 15, 20\}$ km engineering tangent altitudes. We report in Fig. 4 the scatter plots of the vertical and polar tangent point displacements between the ERA5 and the US76 tangent points, with a color gradient representing the position along the orbit.

As shown in the figure, the maximal polar displacement is about 1 km for the 20 km engineering tangent altitudes, and reaches 6 km for the lowest point. In particular, we note a positive correlation between vertical and polar displacements. This fact can be explained in the following way. When the vertical displacement is negative, the ERA5 tangent point altitude is lower than that of the US76 model. Consequently, the ERA5 line of sight must be longer to reach this lower altitude. A longer line of sight implies that the tangent point has a larger orbital shift with respect to the satellite. Since the satellite observes backward along its orbit, this corresponds to a smaller orbital coordinate and therefore a negative polar displacement. In addition, we observe a correlation also between the orbital coordinate and the displacement, independently of the starting longitude of the orbit, as it is visible in the color gradient of the points in the plots of Fig. 4. This suggests a relationship with the latitude bands, and consequently an influence of the climatic conditions.

In order to further investigate this correlation an additional test was performed comparing two orbits covering the same longitudinal band: one acquired on 10 July 2021 at 12:00:00 UTC, and the other on 10 January 2021 at 12:00:00 UTC. We focus on summer and winter, as the seasonal effect is maximized during these periods. We selected a fixed tangent altitude of 5 km as a represen-

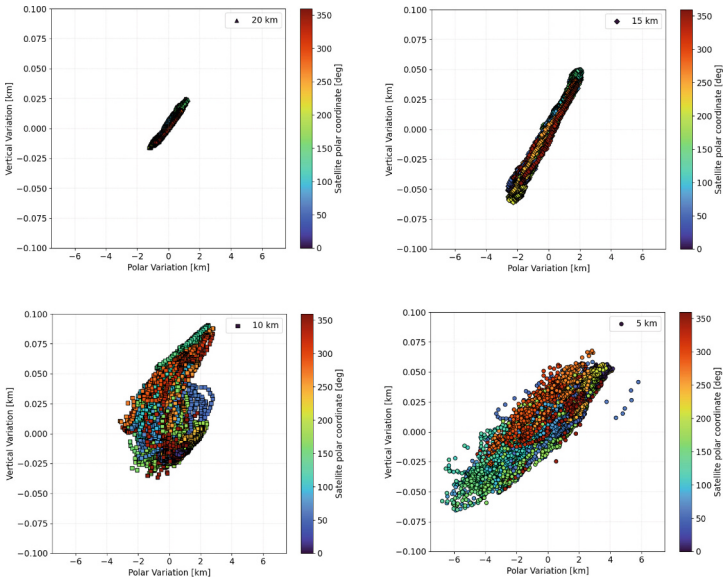

Fig. 4. Scatter plots illustrates the vertical and polar(horizontal) variation of the tangent point from off-nadir angles prediction, calculated as the difference between ERA5 and the US76 atmospheric model, as a function of the satellite's polar angle along the orbit. The plots includes data for four reference altitudes: 5 km, 10 km, 15 km, and 20 km, across 14 orbits.

tative case, since we expect more significant differences from the lowest tangent point. The difference in these two orbits is that the January orbit samples winter conditions in the Northern hemisphere and summer conditions in the Southern hemisphere. The seasonal conditions are reversed for the July orbit.

The results are shown in Fig. 5. The central panel shows the scatterplot of polar and vertical displacements between ERA5 and US76 model. Here, there are no significant differences in this plot. The auxiliary panels display the vertical (left) and polar (bottom) displacements as functions of the satellite's orbital coordinate. Note that, since the instrument looks backward, there is a negative shift of about 25° between the satellite and the tangent point orbital coordinate. Dashed line shows the approximate coordinate when the tangent point crosses the equator, highlighting the orbital intervals where the tangent point samples each hemisphere. As it can be seen there is a correlation between the hemisphere and the sign of both the vertical and polar displacements, confirming our previous assumption. Furthermore, the seasonal effect results in variations of about 5 km in the polar displacement, and of about 50 m in the altitude displacement, highlighting another impact of realistic atmospheric conditions on tangent point localization.

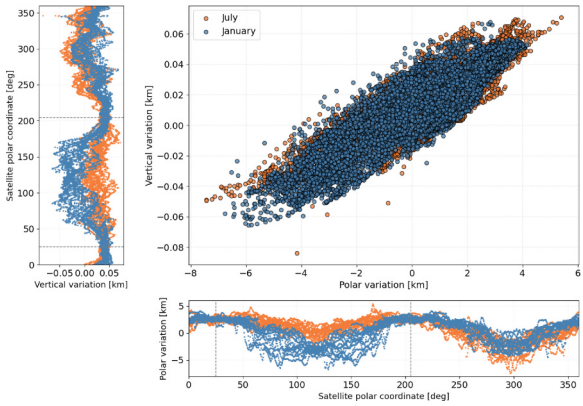

Fig. 5. Scatter plot for the 5 km tangent altitude. The plot shows the seasonal difference for one orbit in July (orange dots) and one orbit in January (blue dots) compares two distinct atmospheric conditions. The differences between the two atmospheric conditions are shown in terms of the vertical and polar variation in the tangent point. Dashed lines at $\sim 25^\circ$ and 205° indicate the approximate tangent point positions near the equator.

4.2 MIPAS Smoothing Error Estimation

The MIPAS Level-2 operational processor *Optimized Retrieval Model* (ORM) [25], is a forward and inversion code that in the last version [8] includes a dedicated ray-tracing module designed for the limb-viewing geometry. A direct comparison between the ORM ray-tracing algorithm and the new algorithm developed for CAIRT is not straightforward, due to fundamental differences in their design.

The ORM employs a different Earth geometry, defined as locally spherical and constructed around the tangent points, which are expressed in fixed polar coordinates. These coordinates are determined a priori by a Level-1 ray-tracing algorithm based on the US76 atmosphere. Each limb scan—defined by a sequence of tangent altitudes along the observation direction—is processed independently within this local spherical framework, where the local Earth radius is calculated from the tangent-point latitude.

More specifically, in the first step of the retrieval, the tangent-point temperatures and pressures for each scan sweep are derived, and the corresponding tangent altitudes are iteratively updated using hydrostatic equilibrium. The ORM ray tracing starts from the tangent point and proceeds bidirectionally up to the top of the atmosphere. In its latest version, ORM also accounts for horizontal gradients to correct biases introduced by the different atmospheric conditions sampled during the ascending and descending parts of the orbit [14].

The ray-tracing algorithm developed for CAIRT instead, as described in Sect. 3, starts from the satellite position and determines the atmospheric entry point along a straight line defined by the given off-nadir angle. The ray path

is then computed by numerically solving the Eikonal Eq. (1) until the line of sight exits the atmosphere. The selected atmospheric model, intersected by the line of sight, is discretized on a curvilinear coordinate system defined by altitude and polar angle along the WGS84 ellipsoid. Additional information regarding the numerical implementation, methodological improvements, and grid geometry can be found in the technical Appendices.

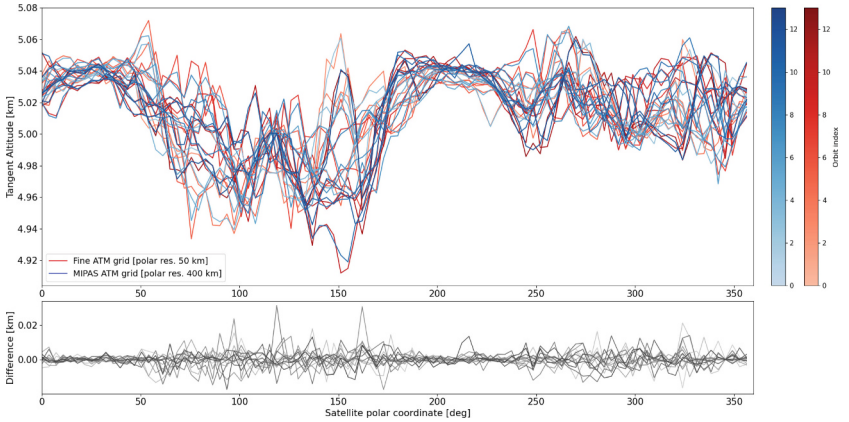

Fig. 6. The plot shows the variation of the tangent point altitude as a function of the satellite's polar coordinate, for a reference tangent altitude of 5 km. The blue curves correspond to values computed using the MIPAS horizontal resolution, while the red curves represent results obtained with a finer atmospheric grid. Tangent heights were evaluated across 14 consecutive satellite orbits, as indicated by the color gradients in blue and red. The subplot presents the residuals, defined as the differences between the tangent altitude estimates derived from the two spatial resolutions.

Our purpose is to quantify the smoothing error introduced by the coarser horizontal resolution of MIPAS acquisitions (about 400 km) compared to the finer sampling achievable with CAIRT (about 50 km). Because of the different approaches in ray tracing, a direct comparison using MIPAS retrieval code is not easy to implement. Thus, we have adopted the following methodology: we discretized the atmosphere using a horizontal grid of 50 km along the WGS84 ellipse, which we assume as the reference *true* atmosphere. This was done by defining the spacing between consecutive polar-angle grid points along the ellipse that form the grid. We then degraded the grid to 400 km, consistent with the horizontal resolution of MIPAS acquisitions. While the grid points are sampled using the same ERA5 data, bilinear interpolation is used to obtain the atmospheric properties needed to compute the refractive index at points within each grid cell. In the coarser resolution, linear interpolation is applied along the polar-angle direction between grid points spaced 400 km, while the interpolation in the altitude direction remains unchanged. This approach is consistent with the Level-2 MIPAS data and reflects how horizontal inhomogeneities are treated in

the ORM. We then compared the ray tracing, using the same MIPAS scan pattern, between the coarse and the fine atmospheric discretization. We assume that the bias due to the coarser resolution is an estimation of the MIPAS smoothing error.

To ensure global coverage, we again examined the set of 14 consecutive orbits already introduced in Subsect. 3.1. The results are presented in Fig. 6. Tangent altitudes computed using the atmosphere sampled at CAIRT resolution are presented in red, while those using the coarser MIPAS resolution are presented in blue. The lower panel shows the differences between the two. We observe that the smoothing error introduced by the MIPAS resolution remains globally below 25 m, an uncertainty directly related to its limited horizontal resolution. This error is much lower than the global uncertainty found in the identification of the tangent altitudes for MIPAS that can reach 200 m [24].

5 Conclusions

Accurate ray tracing is essential in limb-scanning interferometers to account for atmospheric refraction and to precisely determine the tangent point positions. In this paper, we upgraded the MIPAS ray-tracing algorithm, introducing new techniques to solve stability problems and improvements in geometric modeling. We provide the improvement introduced in the algorithm as a reference and use it for two specific analyses.

The first application is on a more accurate study on the relationship between off-nadir angles and tangent points altitudes. The off-nadir angles must be determined a-priori, using either a geometrical model that neglects atmospheric refraction or a standard atmospheric model such as US76. We first show that using the US76 model the predicted and true location of the tangent point are much closer than using the purely geometrical approach, as expected.

Our results show that using off-nadir angles derived from a standard atmosphere leads to tangent point displacements that increase at lower altitudes, reaching up to approximately 100 m in vertical displacement and up to 6 km in the horizontal displacement (i.e., along the polar coordinate of the atmospheric grid), while seasonal variability can introduce additional shifts of up to 50 m vertically and up to 1 km horizontally. This highlights the significant impact of realistic atmospheric conditions on tangent point localization, particularly in the lower troposphere.

In the second application, we estimated the smoothing error due to the coarse 400 km horizontal resolution of MIPAS. The smoothing error was quantified as the displacement of the tangent point when using an atmospheric horizontal grid of 50 km, considered the true state, compared to a 400 km grid, corresponding to the MIPAS resolution. We verified that the altitude error remains globally below 25 m, a value that is lower than the general tangent point error due to the atmosphere of about 200 m as estimated in [24].

Overall, as expected, these results quantify more accurately how using models as close as possible to the true atmospheric state reduces the error in tangent point localization for limb-instruments, particularly in the lower troposphere.

We used the CAIRT mission concept as a case study to explore limb-sounding scenarios where such challenges are expected. Although CAIRT was not selected as an operational mission, the ray-tracing remains relevant for any future limb-scanning missions.

As a final remark, we provide some additional considerations, also from a technical perspective, regarding the computation time.

The time required to compute a single LoS depends primarily on the length of its intersection with the atmosphere. Lower tangent altitudes result in longer atmospheric paths and consequently higher computational costs.

Although the computation time per LoS remains moderate on standard hardware, the large number of LoS paths required by satellite as CAIRT may lead to a computational bottleneck. As a reference, on a standard Intel i7 processor, the ray-tracing code requires approximately 2 h to process a full orbit consisting of 800 acquisitions, each containing 85 LoS.

Further improvements of the ray-tracing algorithm could be envisaged. We foresee two possible approaches:

(i) **Parallelism:** The calculation of each line of sight is independent of the others. A straightforward parallelization of the code should not require any modification to the underlying algorithm, and can be used to reduce the computational time.
(ii) **AI-based methods:** We have shown that off-nadir angles prediction depends also on seasonal variations. To improve the accuracy, this correlation should be incorporated in the atmospheric models, by selecting a climatological atmospheric state that varies with geolocation and time. Machine learning methods trained on a representative dataset can then be used to speed up the computation.

An additional optimization could involve reducing the number of lines of sight explicitly computed by the ray-tracing algorithm. Lines of sight corresponding to nearby engineering tangent altitudes are often strongly correlated, as they traverse nearly identical portions of the atmosphere. Therefore, it may be feasible to interpolate or emulate intermediate lines of sight using machine learning techniques trained on a reduced set of fully computed paths.

However, a key challenge arises from the level of detail required by the forward model: the relevant information is not limited to scalar quantities, but includes the precise geometry and trajectory of each ray path. This geometric fidelity must be preserved to ensure the accuracy of the radiative transfer calculations, making interpolation or emulation non-trivial.

Acknowledgments. The work was conducted within the framework of the CAIRT Analysis and Synergy with IASI-NG (CASIA) project of the Italian Space Agency (ASI), CUP: F93C23000430001.

Disclosure of Interests. The authors have no competing interests to declare that are relevant to the content of this article.

CRediT Authorship Contribution Statement. Francesco Pio De Cosmo: Formal Analysis, Software, Testing, Writing – original draft, Writing – review & editing. **Luca Sgheri:** Methodology, Formal Analysis, Software, Writing – original draft, Writing – review & editing, Funding acquisition.

A Earth and LoS Geometry

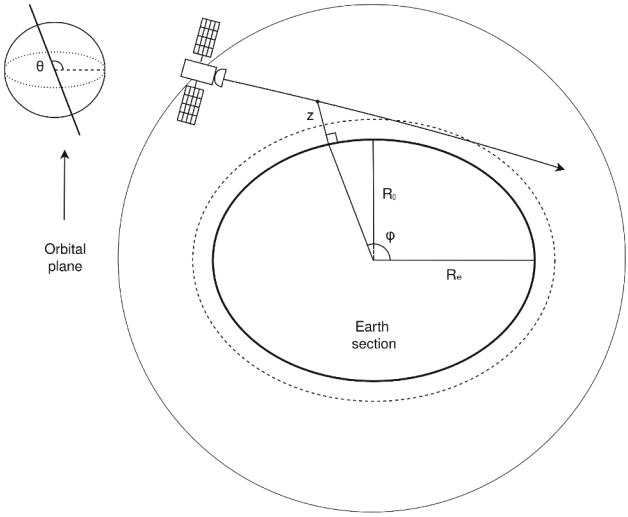

Fig. 7. Observation geometry for a satellite performing limb-viewing in a θ-inclined orbit, illustrating the effect of Earth's oblateness. The figure shows a section of the Earth (WGS84 model) in the satellite's orbital plane. The circle represents the satellite orbit, and the ellipse represents the intersection of the Earth with the orbital plane, with R_e and R_θ denoting the semi-major and semi-minor axes, respectively. The angle φ parameterizes the position of a point on the Earth's surface, and z is its altitude above the surface, measured normal to the ellipse. This allows the points along the line of sight to be expressed in the curvilinear coordinate system (φ, z). Orbit radius and Earth's oblateness are exaggerated for visual clarity.

Earth is represented according to the WGS84 model [19], a rotational ellipsoid with an equatorial (semi-major) radius of $R_e = 6378.137$ km and a polar (semi-minor) radius of $R_p = 6356.752$ km. This choice is essential to avoid large geometric approximations.

As discussed in the main text, the satellite is assumed to move along a circular, sun-synchronous orbit, allowing it to pass over the same Earth location at approximately the same local solar time. Such an orbit defines a plane inclined by an angle θ with respect to the equatorial plane, intersecting the Earth's ellipsoid as illustrated in Fig. 7.

If we restrict our analysis to the orbital plane with inclination θ relative to the equator, the problem can be simplified from three to two dimensions by considering the intersection between the Earth's ellipsoid and the orbital plane. This intersection forms an ellipse whose semi-major axis coincides with the equatorial radius R_e, while the semi-minor axis R_θ depends on the orbital inclination and can be calculated as

$$R_\theta = \sqrt{\frac{R_e^2 R_p^2}{R_p^2 \cos^2\theta + R_e^2 \sin^2\theta}}. \tag{7}$$

We note that $R_\theta = R_e$ for $\theta = 0$ (equatorial direction) and $R_\theta = R_p$ for $\theta = \pi/2$ (polar direction). Within the orbital plane, Earth's surface can be represented by an ellipse centered at Earth's center. In Cartesian coordinates, points on the ellipse can be expressed as $(x(\varphi), y(\varphi)) = (R_e \cos\varphi,\ R_\theta \sin\varphi)$, with $\varphi \in [0, 2\pi]$ the polar parametric angle of Earth's surface. Each point along this ellipse can be mapped to geodetic latitude and longitude, which allows the identification of the sub-satellite position. Atmospheric properties can then be extracted at these locations for a specific UTC.

The computation of the lines of sight extends from the satellite position up to the exit point from the atmosphere. The detectors of course capture the radiation traveling along the line of sight in the opposite direction, reaching the instrument after sampling the atmosphere. Points along these rays, initially calculated from the Eikonal equation in Cartesian coordinates, are then mapped to a curvilinear coordinate system (φ, z), where φ is the polar angle of Earth's surface in the orbital plane and z represents the altitude above the surface, as shown in Fig. 7.

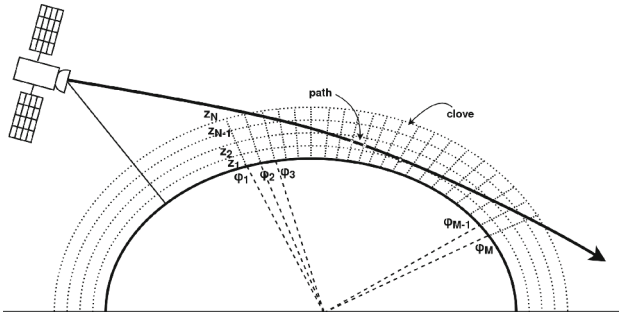

Fig. 8. Atmospheric grid used in the ray-tracing model. The atmosphere is discretized into altitude levels $z_1, \ldots, z_N$ and angular coordinates $\varphi_1, \ldots, \varphi_M$, forming a 2D grid. Each grid cell, called a *clove*, represents a sector of the discretized atmosphere. The segment of a LoS that crosses a clove defines a *path*.

Atmospheric properties are first extracted at sub-satellite geolocations. They are then interpolated into altitude levels $z_1, \ldots, z_N$ and angular coordinates $\varphi_1, \ldots, \varphi_M$, forming a 2D grid $\{\varphi_1, \ldots, \varphi_M;\ z_1, \ldots, z_N\}$, as illustrated in Fig. 8.

This grid defines the curvilinear discretization used in the ray-tracing calculations. A *clove* is defined as a sector of an elliptical annulus, determined by the atmospheric grid nodes, while a *path* corresponds to the intersection of a LoS with a clove. Within each clove, atmospheric properties at intermediate points are obtained by bilinear interpolation of the four surrounding grid points, except for the vertical interpolation in pressure, which follows an exponential rule. These interpolated properties are then used to determine the refractive index, which governs the local curvature of the line of sight. This approach ensures that the discretization captures both horizontal and vertical variations of the atmosphere along the ray path, while maintaining consistency with the underlying curvilinear coordinate system (φ, z).

References

1. Bohren, C.F., Huffman, D.R.: Absorption and Scattering of Light by Small Particles. John Wiley & Sons, New York (1983)
2. Boone, C.D., Bernath, P.F., Walker, K.A., McLeod, S.D.: Ace-fts version 3.6 retrieval updates. J. Quant. Spectroscopy Radiative Transfer **247**, 106939 (2020). https://doi.org/10.1016/j.jqsrt.2020.106939
3. Born, M., et al.: Principles of Optics: Electromagnetic Theory of Propagation, Interference and Diffraction of Light, 7 edn. Cambridge University Press (1999)
4. Buehler, S.A., Eriksson, P.: Microwave limb sounding of the troposphere. In: Platt, U., Stutz, J. (eds.) The Remote Sensing of the Earth's Atmosphere and Surface. University of Bremen Press (2018). https://www.iup.uni-bremen.de/materials/remsensingbook/04_Remote_Sensing_Microwaves.pdf
5. Burrows, J., Hölzle, E., Goede, A., Visser, H., Fricke, W.: Sciamachy–scanning imaging absorption spectrometer for atmospheric chartography. Acta Astronaut. **35**(7), 445–451 (1995). https://doi.org/10.1016/0094-5765(94)00278-T
6. Ciddor, P.E.: Refractive index of air: new equations for the visible and near infrared. Appl. Opt. **35**, 1566–1573 (1996). https://doi.org/10.1364/AO.35.001566
7. Copernicus Atmosphere Monitoring Service (CAMS): Cams global greenhouse gas reanalysis (egg4). https://atmosphere.copernicus.eu/cams-global-greenhouse-gas-reanalysis (2020)
8. Dinelli, M.B., et al.: The esa mipas/envisat level2-v8 dataset: 10 years of measurements retrieved with ORM v8.22. Atmospheric Measure. Techn. **14**(12), 7975–7998 (2021). https://doi.org/10.5194/amt-14-7975-2021
9. Edlén, B.: The refractive index of air. Metrologia **2**, 71–80 (1966). https://doi.org/10.1088/0026-1394/2/2/001
10. ESA: Report for mission selection: Earth explorer 11 candidate mission cairt, european space agency, noordwijk, the netherlands, esa-eopsm-cair-rp-4797, 230 pp (2025). https://doi.org/10.5281/zenodo.15606819
11. European Space Agency: Polar and sun-synchronous orbit (2020). https://www.esa.int/ESA_Multimedia/Images/2020/03/Polar_and_Sun-synchronous_orbit
12. Fischer, H., et al.: Mipas: an instrument for atmospheric and climate research. Atmos. Chem. Phys. **8**(8), 2151–2188 (2008). https://doi.org/10.5194/acp-8-2151-2008
13. Hersbach, H., et al.: The era5 global reanalysis. Q. J. R. Meteorol. Soc. **146**(730), 1999–2049 (2020). https://doi.org/10.1002/qj.3803

14. Kiefer, M., et al.: Impact of temperature field inhomogeneities on the retrieval of atmospheric species from MIPAS IR limb emission spectra. Atmospheric Measure. Techn. **3**, 1487–1507 (2010). https://doi.org/10.5194/amt-3-1487-2010
15. Kiefer, M., et al.: Characterization of mipas elevation pointing. Atmos. Chem. Phys. **7**(5), 1615–1625 (2007). https://doi.org/10.5194/acp-7-1615-2007
16. Livesey, N.: Limb sounding, atmospheric. In: Encyclopedia of Remote Sensing, pp. 344–348. Springer, New York, NY (2014).https://doi.org/10.1007/978-0-387-36699-9_87
17. Mathar, R.J.: Calculated refractivity of water vapor and moist air in the atmospheric window at 10 μm. Appl. Opt. **43**, 928–932 (2004). https://doi.org/10.1364/AO.43.000928
18. NASA Atmospheric Science Data Center: Ace-fts ascii data usage and file format for v3.5 (2016). https://avdc.gsfc.nasa.gov/PDF/ACE-SOC-0026-1B-ACE-FTS_ascii_data_usage_and_fileformat_for_v3.5-15March2016.pdf
19. National Imagery and Mapping Agency: Wgs 84: The world geodetic system 1984 (2000). https://www.ngs.noaa.gov/WGS84/
20. NOAA, NASA, U.S. Air Force: U.S. Standard Atmosphere, 1976. U.S. Government Printing Office, Washington, D.C. (1976). https://ntrs.nasa.gov/citations/19770009539
21. Raspollini, P., et al.: Level 2 processor and auxiliary data for ESA version 8 final full mission analysis of MIPAS measurements on Envisat. Atmospheric Measur. Techn. **15**(6), 1871–1901 (2022). https://doi.org/10.5194/amt-15-1871-2022
22. Read, W.G., Shippony, Z., Snyder, W.V.: Earth observing system (EOS) microwave limb sounder (MLS) forward model: algorithm theoretical basis document. Technical Report JPL D-18130/CL#04-2238, NASA, Jet Propulsion Laboratory, California Institute of Technology, Pasadena, California, USA (2004)
23. Remedios, J.J., et al.: MIPAs reference atmospheres and comparisons to v4.61/v4.62 MIPAs level 2 geophysical data sets. Atmospheric Chemis. Phys. Discuss. **7**, 9973–10017 (2007).https://doi.org/10.5194/acpd-7-9973-2007
24. Ridolfi, M., Sgheri, L.: Characterization of model errors in the calculation of tangent heights for atmospheric infrared limb measurements. Atmospheric Measur. Techn. **7**(12), 4117–4122 (2014). https://doi.org/10.5194/amt-7-4117-2014
25. Ridolfi, M., et al.: Optimized forward model and retrieval scheme for mipas near-real-time data processing. Appl. Opt. **39**(8), 1323–1340 (2000). https://doi.org/10.1364/ao.39.001323
26. Riese, M., et al.: Earth explorer 11 mission candidate cairt: phase 0 system study overview. In: 2023 IEEE International Geoscience and Remote Sensing Symposium (IGARSS), p. 10641615 (2023). https://doi.org/10.1109/IGARSS47720.2023.10641615
27. University of Washington: Strive. https://atmos.uw.edu/strive/ (2025)
28. Waters, J., et al.: The earth observing system microwave limb sounder (EOS MLS) on the aura satellite: a 17-year record of temperature, ozone, and other atmospheric constituents. Atmospheric Measur. Techn. **15**(6), 1583–1610 (2022). https://doi.org/10.5194/amt-15-1583-2022